# Optofluidic chips with nanochannels for dynamic molecular detection using enhanced fluorescence

**P. A. Postigo,[1,*] R. Alvaro,[1] A. Juarros,[2] and S. Merino[2]**

[1]*IMM-Instituto de Microelectrónica de Madrid, IMM-CNM-CSIC, Isaac Newton 8, PTM E-28760 Tres Cantos, Madrid, Spain*
[2]*Micro and Nanofabrication Unit, IK4-Tekniker, 20600 Eibar, Spain*
[*]*pabloaitor.postigo@imm.cnm.csic.es*

**Abstract:** The fabrication of a novel optofluidic chip using nanochannels optimized for DNA-stretched molecules and optical detection by enhanced fluorescence is reported. The chips are composed of a series of microchannels that allow the transport of molecules in the femto-liter per second inside a fluid or gas. The nanochannels are surrounded by a photonic crystal structure to enhance the emission of fluorescent light from the molecules, which can travel along the nanochannel, allowing for enhanced optical detection of the molecules in motion. The photonic crystal structure provides an enhancement up to 2.5 times in the light emitted from fluorescent molecules inside the nanochannels which increases to around 250 when normalized to the area of the nanochannels emitting fluorescence. The results may help to the detection of fluorescent molecules (like marked-DNA) in series by speeding it and allowing the use of less sophisticated equipment.

## References and links

1.  J. O. Tegenfeldt, C. Prinz, H. Cao, R. L. Huang, R. H. Austin, S. Y. Chou, E. C. Cox, and J. C. Sturm, "Micro- and nanofluidics for DNA analysis," Anal. Bioanal. Chem. **378**(7), 1678–1692 (2004).
2.  T. H. H. Le, K. Mawatari, H. Shimizu, and T. Kitamori, "Detection of zeptomole quantities of nonfluorescent molecules in a 10(1) nm nanochannel by thermal lens microscopy," Analyst (Lond.) **139**(11), 2721–2725 (2014).
3.  M. Wanunu, W. Morrison, Y. Rabin, A. Y. Grosberg, and A. Meller, "Electrostatic focusing of unlabelled DNA into nanoscale pores using a salt gradient," Nat. Nanotechnol. **5**(2), 160–165 (2010).
4.  N. Douville, D. Huh, and S. Takayama, "DNA linearization through confinement in nanofluidic channels," Anal. Bioanal. Chem. **391**(7), 2395–2409 (2008).
5.  J. O. Tegenfeldt, C. Prinz, H. Cao, S. Chou, W. W. Reisner, R. Riehn, Y. M. Wang, E. C. Cox, J. C. Sturm, P. Silberzan, and R. H. Austin, "The dynamics of genomic-length DNA molecules in 100-nm channels," Proc. Natl. Acad. Sci. U.S.A. **101**(30), 10979–10983 (2004).
6.  W. Reisner, K. J. Morton, R. Riehn, Y. M. Wang, Z. Yu, M. Rosen, J. C. Sturm, S. Y. Chou, E. Frey, and R. H. Austin, "Statics and dynamics of single DNA molecules confined in nanochannels," Phys. Rev. Lett. **94**(19), 196101 (2005).
7.  W. Reisner, J. P. Beech, N. B. Larsen, H. Flyvbjerg, A. Kristensen, and J. O. Tegenfeldt, "Nanoconfinement-enhanced conformational response of single DNA molecules to changes in ionic environment," Phys. Rev. Lett. **99**(5), 058302 (2007).
8.  E. Abad, A. Juarros, A. Retolaza, S. Merino, R. Marie, and A. Kristensen, "DNA analysis by single molecule stretching in nanofluidic biochips," Microelectron. Eng. **88**(3), 300–304 (2011).
9.  E. Abad, S. Merino, A. Retolaza, and A. Juarros, "Design and fabrication using nanoimprint lithography of a nanofluidic device for DNA stretching applications," Microelectron. Eng. **85**(5-6), 818–821 (2008).
10. Y. M. Wang, J. O. Tegenfeldt, W. Reisner, R. Riehn, X. J. Guan, L. Guo, I. Golding, E. C. Cox, J. Sturm, and R. H. Austin, "Single-molecule studies of repressor-DNA interactions show long-range interactions," Proc. Natl. Acad. Sci. U.S.A. **102**(28), 9796–9801 (2005).
11. R. Riehn, M. Lu, Y. M. Wang, S. F. Lim, E. C. Cox, and R. H. Austin, "Restriction mapping in nanofluidic devices," Proc. Natl. Acad. Sci. U.S.A. **102**(29), 10012–10016 (2005).
12. K. Jo, D. M. Dhingra, T. Odijk, J. J. de Pablo, M. D. Graham, R. Runnheim, D. Forrest, and D. C. Schwartz, "A single-molecule barcoding system using nanoslits for DNA analysis," Proc. Natl. Acad. Sci. U.S.A. **104**(8), 2673–2678 (2007).
13. J. T. Mannion, C. H. Reccius, J. D. Cross, and H. G. Craighead, "Conformational analysis of single DNA molecules undergoing entropically induced motion in nanochannels," Biophys. J. **90**(12), 4538–4545 (2006).

14. C. H. Reccius, S. M. Stavis, J. T. Mannion, L. P. Walker, and H. G. Craighead, "Conformation, length, and speed measurements of electrodynamically stretched DNA in nanochannels," Biophys. J. **95**(1), 273–286 (2008).
15. F. Persson, P. Utko, W. Reisner, N. B. Larsen, and A. Kristensen, "Confinement spectroscopy: probing single DNA molecules with tapered nanochannels," Nano Lett. **9**(4), 1382–1385 (2009).
16. C. Wang, Y. Shi, J. Wang, J. Pang, and X.-H. Xia, "Ultrasensitive protein concentration detection on a micro/nanofluidic enrichment chip using fluorescence quenching," ACS Appl. Mater. Interfaces **7**(12), 6835–6841 (2015).
17. P. Bertone and M. Snyder, "Advances in functional protein microarray technology," FEBS J. **272**(21), 5400–5411 (2005).
18. E. C. Yusko, J. M. Johnson, S. Majd, P. Prangkio, R. C. Rollings, J. Li, J. Yang, and M. Mayer, "Controlling protein translocation through nanopores with bio-inspired fluid walls," Nat. Nanotechnol. **6**(4), 253–260 (2011).
19. C. Merstorf, B. Cressiot, M. Pastoriza-Gallego, A. Oukhaled, J. M. Betton, L. Auvray, and J. Pelta, "Wild type, mutant protein unfolding and phase transition detected by single-nanopore recording," ACS Chem. Biol. **7**(4), 652–658 (2012).
20. M. Soskine, A. Biesemans, B. Moeyaert, S. Cheley, H. Bayley, and G. Maglia, "An engineered ClyA nanopore detects folded target proteins by selective external association and pore entry," Nano Lett. **12**(9), 4895–4900 (2012).
21. J. E. Reiner, J. J. Kasianowicz, B. J. Nablo, and J. W. F. Robertson, "Theory for polymer analysis using nanopore-based single-molecule mass spectrometry," Proc. Natl. Acad. Sci. U.S.A. **107**(27), 12080–12085 (2010).
22. Z. Azad, M. Roushan, and R. Riehn, "DNA Brushing Shoulders: Targeted Looping and Scanning of Large DNA Strands," Nano Lett. **15**(8), 5641–5646 (2015).
23. I. P. Kaminov, H. P. Weber, and E. A. Chandross, "Poly(methyl methacrylate) dye laser with internal diffraction grating resonator," Appl. Phys. Lett. **18**, 497 (1971).
24. M. Imada, A. Chutinan, S. Noda, and M. Mochizuki, "Multidirectionally distributed feedback photonic crystal lasers," Phys. Rev. B **65**(19), 195306 (2002).
25. L. J. Martínez, B. Alén, I. Prieto, J. F. Galisteo-López, M. Galli, L. C. Andreani, C. Seassal, P. Viktorovitch, and P. A. Postigo, "Two-dimensional surface emitting photonic crystal laser with hybrid triangular-graphite structure," Opt. Express **17**(17), 15043–15051 (2009).
26. A. R. Alija, L. J. Martínez, A. García-Martín, M. L. Dotor, D. Golmayo, and P. A. Postigo, "Tuning of spontaneous emission of two-dimensional photonic crystal microcavities by accurate control of slab thickness," Appl. Phys. Lett. **86**(14), 1101–1103 (2005).
27. M. Notomi, H. Suzuki, and T. Tamamura, "Directional lasing oscillation of two-dimensional organic photonic crystal lasers at several photonic band gaps," Appl. Phys. Lett. **78**(10), 1325 (2001).
28. S. Noda, K. Kojima, K. Mitsunaga, K. Kyuma, K. Hamanaka, and T. Nakayama, "Monolithic integration of an AlGaAs/GaAs multiple quantum well distributed feedback laser and a grating coupler for surface emission," Appl. Phys. Lett. **51**, 1200 (1987).
29. L. J. Martinez, A. R. Alija, P. A. Postigo, J. F. Galisteo-López, M. Galli, L. C. Andreani, C. Seassal, and P. Viktorovitch, "Effect of implementation of a Bragg reflector in the photonic band structure of the Suzuki-phase photonic crystal lattice," Opt. Express **16**(12), 8509–8518 (2008).
30. R. H. Pedersen, O. Hansen, and A. Kristensen, "A compact systemforlarge-areathermalnanoimprintlithographyusingsmartstamps," J. Micromech. Microeng. **18**, 5 (2008).
31. V. Chaudhery, S. George, M. Lu, A. Pokhriyal, and B. T. Cunningham, "Nanostructured Surfaces and Detection Instrumentation for Photonic Crystal Enhanced Fluorescence," Sensors (Basel) **13**(5), 5561–5584 (2013).
32. Y.-A. Wu, P.-T. Wu, and C.-S. Huang, "Photonic crystal-enhanced fluorescence through the extraction of dually polarized modes," Opt. Lett. **40**(5), 733–735 (2015).
33. Y. Tan, T. Tang, H. Xu, C. Zhu, and B. T. Cunningham, "High sensitivity automated multiplexed immunoassays using photonic crystal enhanced fluorescence microfluidic system," Biosens. Bioelectron. **73**, 32–40 (2015).
34. Y. K. Xu, S. Hwang, S. Kim, and J. Y. Chen, "Two orders of magnitude fluorescence enhancement of aluminum phthalocyanines by gold nanocubes: a remarkable improvement for cancer cell imaging and detection," ACS Appl. Mater. Interfaces **6**(8), 5619–5628 (2014).
35. A. Puchkova, C. Vietz, E. Pibiri, B. Wünsch, M. Sanz Paz, G. P. Acuna, and P. Tinnefeld, "DNA Origami Nanoantennas with over 5000-fold Fluorescence Enhancement and Single-Molecule Detection at 25 μM," Nano Lett. **15**(12), 8354–8359 (2015).
36. P. Strobbia, E. Languirand, and B. M. Cullum, "Recent advances in plasmonic nanostructures for sensing: a review," Opt. Eng. **54**(10), 100902 (2015).
37. W. H. De Jong, L. T. Van Der Ven, A. Sleijffers, M. V. Park, E. H. Jansen, H. Van Loveren, and R. J. Vandebriel, "Systemic and immunotoxicity of silver nanoparticles in an intravenous 28 days repeated dose toxicity study in rats," Biomaterials **34**(33), 8333–8343 (2013).

## 1. Introduction

There is a need for reducing dimensions and for increasing sensitivity of analytical testing devices of biological samples. Advances in micro- and nanofluidics have resulted in higher throughput analysis of biologically active processes at a fraction of the speed and cost,

compared to traditional approaches [1]. The ultimate goal for these microdevices is to reach sensitivities at the molecular level [2]. DNA molecules are one of the most important examples for molecular detection. Current methods for DNA analysis are expensive and slow, requiring cutting each molecule into millions of fragments, replicating each segment, classifying them by size and reconstructing the original DNA chain. In contrast, methods based on single molecule detection and DNA stretching of individual molecules by confinement in nanofluidic channels, open new possibilities for DNA analysis [3,4] and detection biochemistry, speeding the process and reducing the cost. These nanofluidic devices have been used for real-time measurement of the contour of the stretched DNA molecules [5–9], protein interaction studies and DNA [10], the orderly organization using endonucleases [11], identification of individual molecules DNA using nanoslits [12], entropic movement and speed of stretched DNA molecules in nanochannels [13,14] and spectroscopy of individual DNA molecules confined in nanochannels [15]. In parallel, chips for detection of a single protein inside micro and nanofluidics [16] are showing promising results. Thus, the combination of nanopores (2-100 nm) coupled to an electric field has proved to be an instrumental tool for studying protein translocation [17], protein conformational changes [18] or to study the presence of native proteins covalently bound to aptamers near the nanopore [19]. Most of these molecular devices analyze the fluorescence signal from a single molecule [21,22] either as a direct measure of molecular detection or as a proxy to study the passage of a molecule through a nanopore or nanochannel even when an electric signal is detected. In this case, the molecular detection requires advanced equipment to collect the faint fluorescent signals emitted by a single individual molecule (stained with a fluorophore, quantum dot or other luminescent label) interposed. Typically highly sensitive cameras, such us an electron multiplying charged coupled device (EMCCD) are used for this purpose. Therefore, obtaining large ratios of the optical signal to noise is crucial for faster and more accurate detection.

In this work we demonstrate the increase of signal detection through the use of specially designed photonic structures coupled to fluidic nanochannels in a chip. Specific photonic structures -like photonic crystals- can be fabricated around the nanochannels (where the molecules travel) with the goal of redirecting the fluorescent light to specific directions where the detection device is placed. The photonic crystal structures recover the fluorescence confined in the plane of the chip (that otherwise would be lost) and promote its emission in the direction of the detection (vertical to the chip). In this work we demonstrate that using photonic crystal structures around the nanochannels allowed for an enhancement in the detection of fluorescent light of more than two orders of magnitude. This improvement may ultimately help to the enhanced detection of individual molecules (like DNA) without the need for sophisticated detection equipment and facilitating the use of these devices for detecting biomolecules in series and in less time. Our device uses a photonic crystal structure made of a two-dimensional (2-D) periodic array of nanoholes specifically designed to provide an optical resonance that matches the emission wavelength of the fluorophore, quantum dot or fluorescent molecule moving inside the nanochannel. The photonic crystal is designed to promote the distributed optical feedback effect (DFB) in the plane of the chip where the nanochannels are embedded [23] thus recovering light otherwise lost and redirecting it to the vertical direction where the detection system is placed. In one dimension (i.e. in a 1-D periodic structure as for example a diffraction grating) the DFB effect results in a coupling of two waves in two opposite directions (propagating and counter-propagating). The effect in 2-D increases the efficiency of the feedback, and it has been successfully demonstrated in photonic crystal microlasers [24]. Our device makes use of 2-D DFB diffraction by means of 2-D photonic crystal structures around the nanochannels. We optimized the dimensions of the nanochannels for the stretching of DNA molecules [8,9] allowing for the movement of the molecules through them inside a carrying fluid.

## 2. Photonic crystal design for enhanced detection of fluorescence

Figure 1 shows a schematic drawing of the chips. The wafer is composed of 3 layers that form an optical waveguide: a core layer of high refractive index ($Si_3N_4$), a lower layer for optical isolation ($SiO_2$) and a third upper cladding layer to seal the nanochannels (Pyrex).
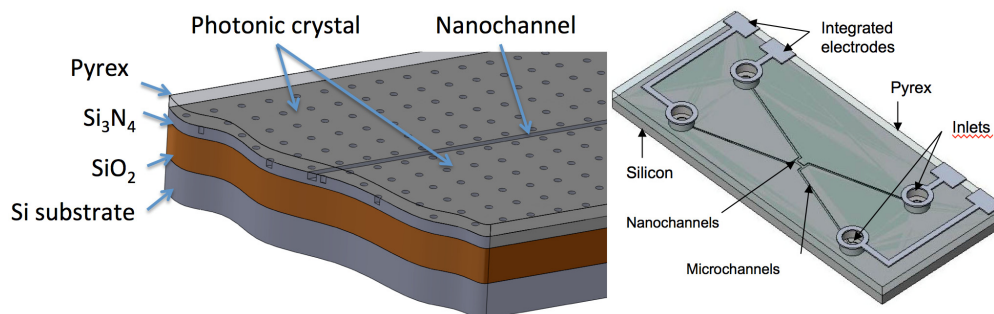


Fig. 1. Schematic drawing of the fabricated chips. The area containing the nanochannels appears magnified in the bottom panel. The chip contains two microchannels with inlets and outlets for the introduction of the carrying fluid with the fluorescent molecules. They are fabricated on a silicon 4-inch wafer and sealed with a pyrex 4-inch wafer on top.

The $SiO_2$ layer is necessary to promote the optical confinement of the fluorescence in the $Si_3N_4$ core layer [25, 26]. The core layer contains the nanochannels with submicronic dimensions specially designed to transport fluids or gases in flows of 10 fL/s [8,9]. The photonic crystal structures that allow for the photon recycling by the DFB effect are fabricated in this layer on both sides of the nanochannels. The distance between the nanochannel and the nearest row of nanoholes is the same than the lattice period of the photonic crystal. Since the three layers forms an optical waveguide, transverse electric and magnetic modes (TM and TE) can be defined [27]. Figure 2 shows the photonic band diagram for the TE and TM modes of an optical waveguide (effective index $n = 1.5$) with a photonic crystal formed by a periodic network of circular nanoholes with triangular symmetry. The holes are filled by air and have radius $r = 0.3a$ where $a$ is the photonic crystal lattice parameter (separation between centers). At the edges of the photonic crystal Brillouin zone, the propagating waves are coupled, significantly increasing the density of optical modes.
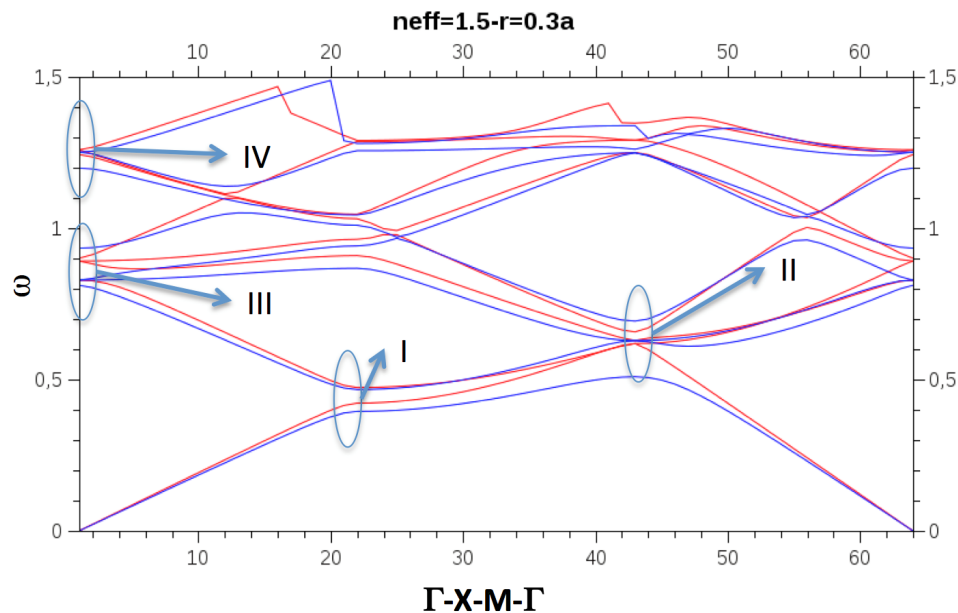
Fig. 2. Photonic band dispersion diagram of the TE(blue) and TM (red) modes for an effective index $n = 1.5$ and holes with $r = 0.3a$. The different areas for the DFB effect are labeled (I to IV) and discussed in the text.

This coupling is different for each point according to Bragg conditions [23]. Our photonic crystal is designed to enhance both TE and TM modes so a higher number of photonic modes can be used for the DFB effect.

In Fig. 2 the point I corresponds to the overlap of only two waves, propagating and counter-propagating, traveling in opposite directions. This type of coupling is similar to what occurs in DFB lasers. Since there are 6 equivalents directions of the Γ-X type, the formation of three different optical resonances in three different directions is allowed. The point II in Fig. 2 has characteristics of a unique coupling that cannot be achieved in conventional DFB lasers, as is the coupling of waves propagating in three directions [27]. The Γ-J direction also exists in each of the six possible directions so that there are only two independent resonances of the DFB type. Nevertheless the applicability of this mode is uncertain because the light is emitted in three different directions. The point III has a wavevector $k = 0$ (i.e. vertical emission) and is related to the coupling of waves propagating in six possible directions. This is the best choice because it includes the coupling within the plane in six directions ($0°, \pm 60, \pm 120°$ and $180°$) inside the plane. Furthermore the direction of the resultant vector of coupling is perpendicular to the plane of the photonic crystal according to the first order Bragg diffraction [23, 28]. In our device this effect is used for the recovery of light emitted in the six directions of the plane formed by the photonic crystal. There are other places at higher frequencies where a multidirectional wave coupling occurs, like the point IV. However the angles of the outgoing directions of the plane of the photonic crystal are not near the normal or close to it. Therefore the most favorable for maximum recovery of light due to the effect DFB is the point III.

Figure 3(a) shows the band diagram for the TE and TM modes for a range of near point III normalized frequency ($\omega$) ranging from 0.6 to 1, $n = 1.62$ and $r = 0.25a$ (triangular symmetry). This diagram can be used to define the range of the useful energy of the device. Ideally the spectral range of the emission of the fluorophore must be within the frequency range defined by the lowest and highest value of the frequency of the bands in $k = 0$ (Γ-point) where the vertical emission occurs (i.e., perpendicular to the plane of the photonic crystal).

From Fig. 3(a) this range is between $\omega = 0.7$ and $\omega = 0.925$ (the bands inside the black square). Since $\omega = a/\lambda$ and $\lambda$ is the wavelength of the emission of the fluorophore, we can extract the value of $a$ (for a fixed $r$). If the spectral width of the emission fluorescence is between wavelengths $\lambda_1$ and $\lambda_2$, we can define the average value as $\lambda_{av} = (\lambda_1 + \lambda_2)/2$ which is typically the approximate value of the wavelength with a higher emission intensity of a Lorentzian emitter. In our device this value must match the average value of the range mentioned above, which according to Fig. 3(a) is $(0.925 + 0.7)/2 = 0.8125$. This implies that the optimum value of the normalized frequency is around 0.8 and hence the lattice parameter value $a$ required to produce the photonic crystal can be obtained from $\omega = a/\lambda_{av}$. All the TE and TM photonic modes shown in Fig. 3 are likely to radiate vertically through the DFB effect at the energy defined at the point $\Gamma$ ($k = 0$). Depending on the symmetry of the lattice photonic crystal (square or triangular or other) the distance between the nanochannel and the nearest row of holes changes. For a maximum DFB effect in the nanochannel, the separation between the nanochannel and the nearest holes must be a multiple of $a$. We note that about half of the light is diffracted in the opposite direction (to the silicon substrate) by the photonic structure. In many photonic crystal structures the z-symmetry of the waveguide (i.e. the specular symmetry along a horizontal plane containing the photonic crystal) cancels the contribution of the TM modes. In our case the z-symmetry is broken, thanks to an adequate separation between the layer of $SiO_2$ and the silicon substrate, so that TM modes can contribute also to the recovering of light [29]. This is important since, in general, the fluorescent emitter can emit photons with a mixed TE and TM polarization. Figure 3(b) shows the photonic bands near the point III for a photonic crystal with $n = 1.7$ and $r = 0.25a$ (square symmetry). The effective index corresponds to an optical guide formed by a layer 170nm thick $Si_3N_4$ sandwiched between a $SiO_2$ layer (500 nm) and a Pyrex layer with an infinite thickness, close to the real case. Figure 3(b) shows a total of 8 photonic modes (TE and TM polarized) near the point III that can contribute to the DFB effect. The $Si_3N_4$ has a refractive index $n = 2$ for a wavelength $\lambda = 514$nm, which is the wavelength of maximum intensity for the fluorophore that we have used as a test. Despite the square and triangular geometries can be good for an initial proof of concept, an ideal geometry should provide as many as possible photonic bands with DFB effect in the spectral range of interest and $k = 0$. This spectral range can be tuned by varying the $r$ and $a$ parameters of the photonic lattice.
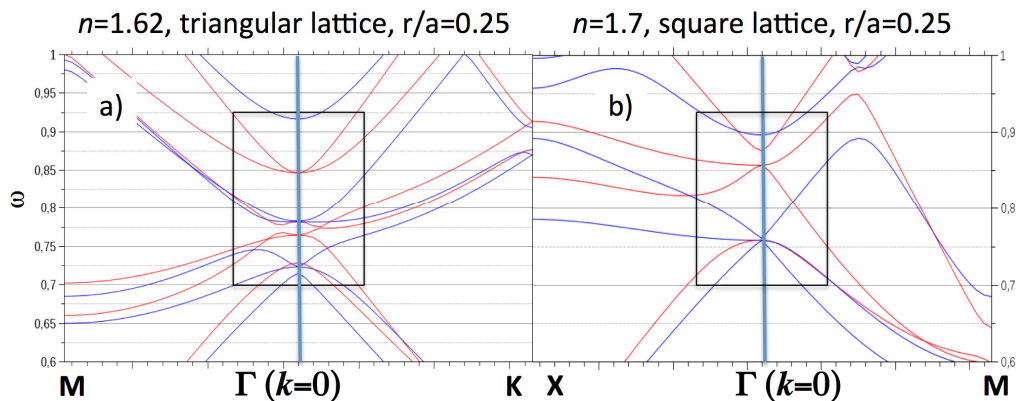


Fig. 3. a) Photonic band dispersion diagram of the TE(blue) and TM (red) modes for an effective index $n = 1.62$ and holes with $r = 0.25a$. The photonic bands contributing to the point III-related DFB effect are inside the black rectangle. b) Square lattice symmetry and $n = 1.7$.

## 3. Fabrication and characterization

The device is manufactured on a silicon wafer on which a silicon oxide layer ($SiO_2$) of 500 nm and another layer of silicon nitride ($Si_3N_4$) of thickness 170nm, have been deposited by

plasma enhanced chemical vapor deposition (PECVD). Each device has 4 input and output ports for injecting fluids, and 2 V-shaped microchannels for the transport of fluid to the entrance of the nanochannels. The microchannels are of 200μm width and depth 3μm and have been manufactured by photolithography techniques and Deep Reactive Ion Etching (DRIE). The device contains a total of 6 nanochannels of 500μm in length, width $w$ = 100nm and depth $h$ = 100 nm. We have alternately included photonic crystals to compare the light emitted from nanochannels with and without the photonic structures. We have used square and triangular symmetry of the photonic crystal to explore its effect. The nanochannel #1 has a photonic crystal with a square lattice of parameter $a$ = 354nm, and radius of the holes $r$ = 71nm. Nanochannel #2 has no photonic structure. The nanochannel #3 is the same as 1 with $a$ = 400 nm, $r$ = 100nm. Nanochannel #4 has a photonic crystal with triangular symmetry and lattice parameter $a$ = 447nm, $r$ = 89nm. Nanochannel #5 has no photonic structure. Finally the nanochannel #6 has a photonic crystal triangular lattice with $a$ = 467nm, $r$ = 93nm. The nanochannels and the photonic crystals are machined by focused ion beam (FIB) in the same fabrication step for a proof of concept, although other methods like nanoimprint could be used for a faster fabrication integrating micro and nanopatterns in one single step [30]. The device is sealed by anodic bonding using a Pyrex wafer 500μm thick and previously machined with four through holes of 1 mm diameter using a femtosecond laser. Figure 4 shows the device images on different scales. Panel (a) shows an image obtained by optical microscopy (500X) where the two V-microchannels can be seen. The 6 above described nanochannels are located between the microchannels. Panel (b) shows an image of scanning electron microscopy (SEM) in the area of the nanochannels, where nanochannels #1 to #6 are visible. The panel (c) is a SEM image of nanochannel #2 (without photonic crystal) and #3 (with photonic crystal). Panel (d) is an image of atomic force microscopy (AFM) of the nanochannel #3 showing the photonic crystal structure on both sides of the nanochannel.
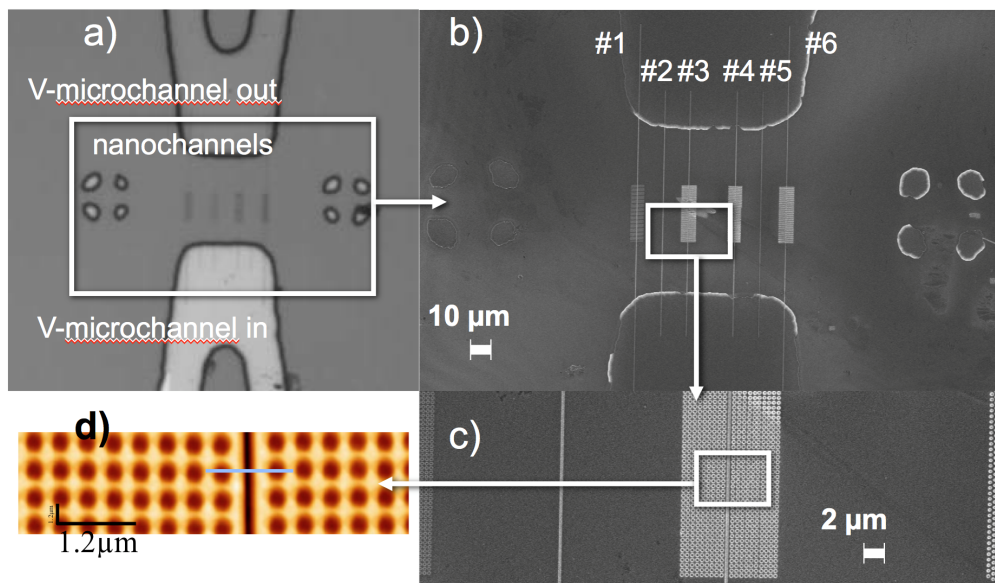


Fig. 4. Scanning electron microscopy (SEM) images of the chips fabricated. The magnification of the areas marked by the white rectangles (a, b and c) is sequentially increased. The image in (d) is anatomic force microscopy (AFM) image of the area marked by the white box in c). The nanochannels are labeled from #1 to #6.

For the optical characterization of the chip performance we have used fluorophore molecules of compound 46960 Fluka Fluorescein sodium salt ($\lambda_{exc}$ = 490 nm, $\lambda_{emiss}$ = 514 nm) inside a carrying fluid 0.1M Tris pH 8.0 which are introduced into the chip through the ports

using a syringe. Once injected through the inlet port, the fluorophore easily filled the microchannels by capillary action to reach the entrance of the nanochannels. The excitation of the fluorophore molecules travelling inside the nanochannels is performed by a 100W HBO Hg-lamp that is part of the microscope used for the imaging [8,9].
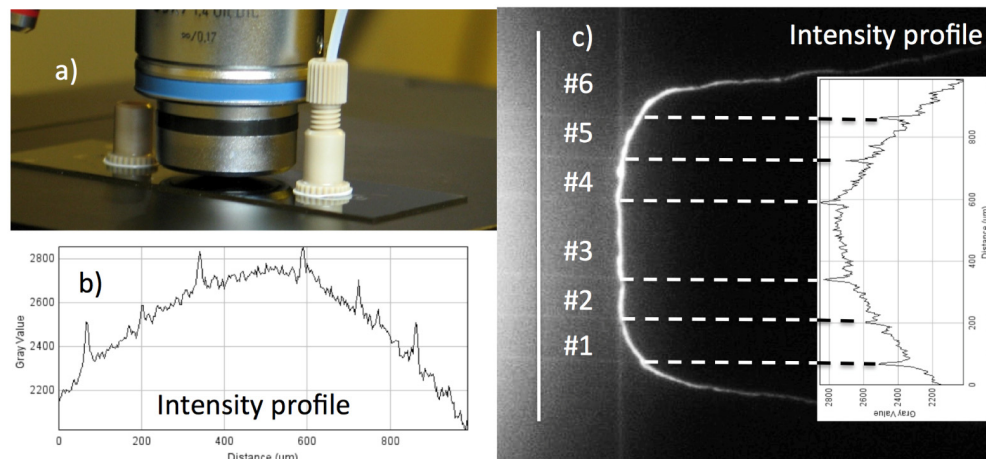


Fig. 5. a) Experimental setup used for detection of the fluorescence. (b) Intensity of the fluorescence vs. the position recorded along the vertical white line shown in (c). (c) SEM image of the nanochannels labeled from #1 to #6. The peaks observed in the intensity profile correspond to the position of the nanochannels.

A pressure of 1 bar is applied with an external injection pump, so that the compound passes through the nanochannels fluorophore with an approximate flow rate of 10 fl/s. The device is placed under a reflection microscope (Zeiss) using 10X and 50X objective magnification, a filter set (BPexc 470/40 (HE), FT 495 (HE), BPEM 525/50 (HE)) and an EMCCD high sensitivity camera (Photometrics Evolve).

Light from the Hg-lamp passes through the filter set (38HE) illuminating the area of the nanochannels and exciting the fluorophore compound in a range of wavelengths from $\lambda =$ 450nm to 490nm. The fluorophore emits with a maximum in the wavelength $\lambda = 514$nm. Figure 5 shows the experimental setup used for the characterization of the fluorescence and a microscopy image of the device with the fluorophore injected and flowing through the nanochannels towards the receipting V-microchannel. An intensity profile of the fluorescence detected is made by software analysis along the vertical white line shown in Fig. 5(c). The profile represents the intensity of the light detected by the EMCCD camera according to the pixel number (position). The profile has a Gaussian shape corresponding to the distribution of background light that comes from the microchannel and a series of peaks that coincide in position with each of the nanochannels. These peaks are produced by the extra amount of light emitted by the fluorescent molecules inside the nanochannel. Figure 6 shows several of such profiles taken along different lines parallel to the white line of Fig. 5(c), i.e., perpendicular to the nanochannels. The values shown in Fig. 6 are the average values taken from 9 intensity versus pixel sections parallel to the white line. A quantification of the error can be extracted using the emission of nanochannels #2 and #5 that do not have photonic crystal structures providing a standard deviation $\sigma = 17$. The first observation is that all the nanochannels with the photonic crystals show a clear improvement compared to the nanochannels without them. The intensity of light from the nanochannels #1, #3, #4 and #6 (which have photonic crystal structures) is in average a 40% higher than the intensity of the nanochannels #2 and #5 that do not have around any photonic structure. The intensity in the nanochannel #1 shows in average a 250% increase in light intensity compared to nanochannel #2 (without photonic structure). The second best structure is nanochannel #6 (with a 2.1 factor

in improvement, which intensity is similar to #1) followed by #6 and #3 (with similar intensities in average) with enhancements of 1.9 and 1.5 compared to nanochannel #2. If we average the intensity of the nanochannels without photonic crystal (i.e., #2 and #5) the enhancements range from 1.3 to 1.9. Performance of nanochannel #4 is the poorest which is probably related to a non-optimized value of the (r,a) parameters. This points out the importance of the selection of those values for a specific photonic crystal. It is observed that the photonic crystal symmetry (triangular or square) does not appear to have a significant role, which we attribute to a similar density of states in the spectral region of interest. We note that the increase cannot be attributed to reflection of light in the silicon substrate since we are comparing between nanochannels with and without photonic crystals and closely fabricated one to the other. Moreover, it is remarkable that the increase is consistent and well correlated with the presence of the photonic crystal structures. Previous works using photonic crystals for light extraction have shown enhancements of the detected fluorescence between 3.8 and 20-fold [31–33]. We notice that in such experiments the photonic crystal is only one-dimensional (i.e., a diffraction grating) and what is even more important, the photonic crystal area entirely covers the area of the fluorescent emission. In our case the area of light emission (i.e., the nanochannels) is 100 times smaller than the area of the photonic crystal used. Therefore and due to the small area of our light source (the nanochannel) the enhancement ratio per unit area is around 250, which is the highest value per unit area reported in the literature for a non-plasmonic effect. Plasmonic enhancements of fluorescence in the range from hundreds to thousands have been reported using nanoparticles [34], nanoantennas [35], or other approaches [36]. Our device shows a smaller enhancement but it is free of metals or metallic nanoparticles, which may cause problems of toxicity during biodetection essays [37].
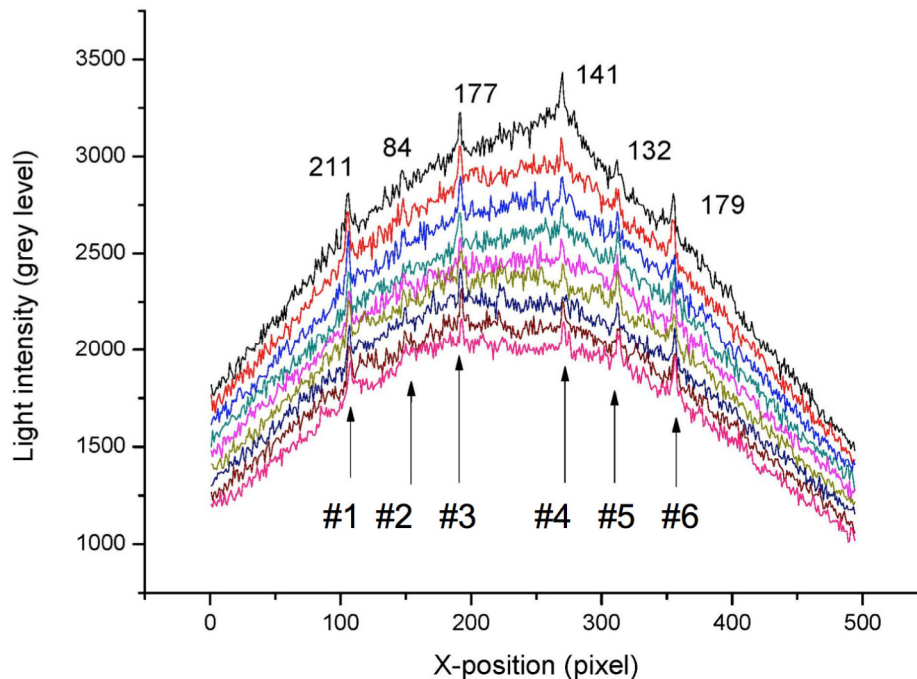


Fig. 6. Profiles of the intensity of fluorescence vs. the position (pixel number) in the chip, recorded for different sections perpendicular to the nanochannels. The peaks correspond to the nanochannels #1 to #6. The number on top of the peaks gives the average value of the intensity for each of the peaks.

Moreover, plasmonic enhancements are strongly dependent on the shape of the nanoparticle and on the local concentration, both difficult to control. Our device provides

enhancement on a broader range that can be finely tuned by the photonic crystal parameters. The observed increase in the detected light may bring important benefits like the use of a less sensitive CCD camera or using a shorter integration time for the detection. The research work described in this article is focused in the analysis and comparison of different photonic crystal designs in order to enhance the detection of fluorescence. Aspects as detection limit and range of detection will be analysed in future experiments using different concentrations of fluka or adding fluorescent-labeled DNA now that the expected results have been experimentally validated.

## 4. Conclusions

We have designed, fabricated and characterized a silicon-based optofluidic chip incorporating micro and nanochannels for the motion of fluids and fluorescent molecules or fluorophores. The nanochannels have been fabricated with surrounding photonic crystals to enhance the detection of fluorescence by redirecting it towards the vertical direction using the DFB effect. Optical characterization shows an average increase in the fluorescence detected of 40% and up to 2.5 times for one of the photonic crystal structures. If we take in account that the actual area that emits light is restricted to that of the nanochannels, the increase per unit area is around 250, which is one of the highest reported. Further work may be related with the optimization of the photonic crystal structure for a specific fluorescent molecule. We believe that the results ultimately may help the detection of individual molecules (like fluorescent marked-DNA) without the need for sophisticated detection equipment, in series and in less time.

## Funding

## Acknowledgments